



**Effects of Antiferroelectric Substitution on the Structure and Ferroelectric Properties of a Complex Perovskite Solid Solution**

Journal:	<i>Journal of Materials Chemistry C</i>
Manuscript ID	TC-ART-09-2019-005084.R4
Article Type:	Paper
Date Submitted by the Author:	18-Mar-2020
Complete List of Authors:	<p>Liu, Zenghui; Xi'an Jiaotong University, ; Simon Fraser University , Department of Chemistry          Yuan, Yi; Simon Fraser University          Luo, Zeng; Xi'an Jiaotong University          Wan, Hongyan; Xi'an Jiaotong University          Gao, Pan; Xi'an Jiaotong University          Wu, Hua; Donghua University, Applied Physics          Zhuang, Jian; Xi'an Jiaotong University,          Zhang, Jie; Xi'an Jiaotong University, Electronic Materials Research Laboratory, Key Laboratory of the Ministry of Education &amp; International Center for Dielectric Research; Xi'an Jiaotong University, Electronic Materials Research Laboratory, Key Laboratory of the Ministry of Education &amp; International Center for Dielectric Research          Zhang, Nan; Xi'an Jiaotong University, a. Electronic Materials Research Laboratory, Key Laboratory of the Ministry of Education &amp; International Center for Dielectric Research          Liu, Hongzhong; Xi'an Jiaotong University, State Key Laboratory for Manufacturing Systems Engineering          Ren, Wei; Xi'an Jiaotong University,          Ye, Zuo-Guang; Simon Fraser University, Chemistry</p>

# Effects of Antiferroelectric Substitution on the Structure and Ferroelectric Properties of a Complex Perovskite Solid Solution

Zenghui Liu<sup>1,2</sup>, Yi Yuan<sup>2</sup>, Zeng Luo<sup>1</sup>, Hongyan Wan<sup>1</sup>, Pan Gao<sup>3,1</sup>, Hua Wu<sup>4,2\*</sup>, Jian Zhuang<sup>1</sup>, Jie Zhang<sup>1</sup>, Nan Zhang<sup>1</sup>, Hongzhong Liu<sup>5</sup>, Wei Ren<sup>1\*</sup>, and Zuo-Guang Ye<sup>2\*</sup>

<sup>1</sup> Electronic Materials Research Laboratory, Key Laboratory of the Ministry of Education & International Center for Dielectric Research, School of Electronic and Information Engineering, Xi'an Jiaotong University, Xi'an 710049, China

<sup>2</sup> Department of Chemistry and 4D LABS, Simon Fraser University, Burnaby, British Columbia V5A 1S6, Canada

<sup>3</sup> School of Electronic Information & Artificial Intelligence, Shaanxi University of Science and Technology, Xi'an 710021, China

<sup>4</sup> Department of Applied Physics, Donghua University, Ren Min Road 2999, Songjiang, 201620 Shanghai, China

<sup>5</sup> State Key Laboratory for Manufacturing Systems Engineering, Xi'an Jiaotong University, Xi'an, Shaanxi, 710049, China

\* Email addresses: [zye@sfu.ca](mailto:zye@sfu.ca), [wuhua@dhu.edu.cn](mailto:wuhua@dhu.edu.cn), and [wren@xjtu.edu.cn](mailto:wren@xjtu.edu.cn)

## Abstract

Ferro-/piezoelectric materials are crucial for a wide range of technologically important devices including electromechanical sensors and actuators and nonvolatile memory. In order to design new materials with high performance and high Curie temperature and to understand the underlying relationship between the structure and properties, a novel solid solution of complex perovskite structure was synthesized in the form of ceramics by the solid-state reaction method. The effects of the substitution of antiferroelectric PbZrO<sub>3</sub> (PZ) on the crystal structure, phase transitions, and

dielectric and piezo-/ferroelectric properties of the  $\text{Bi}(\text{Zn}_{2/3}\text{Nb}_{1/3})\text{O}_3\text{-PbTiO}_3$  (BZN-PT) binary solid solution were studied. The phase transformation sequences of tetragonal ferroelectric phase  $\rightarrow$  rhombohedral ferroelectric phase  $\rightarrow$  orthorhombic antiferroelectric phase with a PZT-like morphotropic phase boundary (MPB) between the tetragonal and rhombohedral phases were indicated by X-ray diffraction and various electric measurements. A pseudobinary phase diagram delimiting the various phase regions was established by a combination of dielectric measurements, X-ray diffraction and selected area electron diffraction (SAED). Attractive electrical properties with  $d_{33} = 260$  pC/N,  $k_p = 0.41$ ,  $P_r = 31.2$   $\mu\text{C}/\text{cm}^2$ ,  $E_C = 16$  kV/cm,  $T_C = 281$   $^\circ\text{C}$  and  $T_{\text{MPB}} = 214$   $^\circ\text{C}$  were obtained for the composition of  $x = 0.5$ , which is in the MPB region. Complex domain structure was found in this solid solution. Most importantly, the high piezoelectric properties obtained in the MPB composition was determined to arise from the significantly enhanced intrinsic contribution as evidenced by the piezoresponse force microscopy (PFM). The enhanced electrical properties with a high  $T_C$  and in particular a high  $T_{\text{MPB}}$  in  $(1-x)(0.2\text{BZN}-0.8\text{PT})-x\text{PZ}$  arise from the combined effect of the MPB, the stereochemically active lone pair electrons on  $\text{Bi}^{3+}$  and the ferroelectrically active cations of  $\text{Zn}^{2+}$  and  $\text{Nb}^{5+}$ , making it a novel piezoelectric material for electromechanical transducer applications. This work helps better understand the origin of the high piezoelectricity in bismuth-based solid solutions and opens up further investigation into other bismuth-based solid solutions that could exhibit higher piezo-/ferroelectric performance.

**Keywords:** PZT, Bismuth-based solid solution, Morphotropic phase boundary, Domain structure, Piezoelectric and ferroelectric properties

## Introduction

Ferro-/piezoelectric materials have been utilized in a wide variety of technologically important devices, including sensors, actuators, medical ultrasound imaging transducers, electromechanical motors and sonar systems<sup>1-7</sup>. Among all the

ferro-/piezoelectric materials, lead zirconate titanate  $\text{Pb}(\text{Zr}_x\text{Ti}_{1-x})\text{O}_3$  (PZT) ceramics, one of the most important commercially produced piezoelectric materials, have attracted special attention due to their high piezoelectric response for the compositions in the vicinity of the morphotropic phase boundary (MPB) <sup>8, 9</sup> With the increase of  $\text{PbTiO}_3$  concentration, PZT shows a composition-driven structural transformation from orthorhombic symmetry to rhombohedral symmetry to tetragonal symmetry. The MPB was found to exist between the rhombohedral phase and the tetragonal phase at around  $x = 0.52 - 0.55$  <sup>9-15</sup> and believed to facilitate the polarization rotation to induce excellent piezoelectricity in PZT <sup>16-18</sup>. However, the Curie temperature ( $T_C$ ) of PZT is relatively low ( $T_C \approx 360 - 380$  °C), which restricts the applications of PZT in extremely high temperatures as the proper functioning temperature is generally limited to half of  $T_C$  <sup>19</sup>.

In recent years, growing interest has been attracted to bismuth-based perovskites because of their reduced toxicity and the enhanced crystal distortion/electrical polarization and  $T_C$  arising from the stereochemically active lone pair electrons. For example, excellent piezoelectric performance with  $d_{33} \approx 460$  pC/N and a high  $T_C$  of 450 °C were found in  $(1-x)\text{BiScO}_3-x\text{PbTiO}_3$  [(1-x)BS-xPT] solid solutions at the MPB <sup>20</sup>. Moreover, Suchomel *et al.* observed a  $T_C$  up to 700 °C and an ultra-large tetragonality  $c/a \approx 1.11$  (with  $a$  and  $c$  the lattice parameters) in the tetragonal  $(1-x)\text{Bi}(\text{Zn}_{1/2}\text{Ti}_{1/2})\text{O}_3-x\text{PbTiO}_3$  [(1-x)BZT-xPT] crystal before reaching its solubility limit at  $x = 0.6$  <sup>21</sup>. Inspired by these attractive systems, a few significant researches have been carried out to study the ferro-/piezoelectric properties in bismuth-based ternary solid solution systems. For instance, Sehirlioglu *et al.*, successfully constructed a ternary MPB by combining the binary MPBs of PZ-PT and BS-PT in the BS-PZ-PT ternary system, where a large-signal piezoelectric coefficient ( $d_{33}^*$ ) higher than 400 pm/V and a high  $T_C$  up to ~400 °C can be obtained <sup>22</sup>.

Lately, our group has extensively investigated  $\text{Bi}(\text{Zn}_{2/3}\text{Nb}_{1/3})\text{O}_3$  based solid solutions, which have ferroelectrically active  $\text{Zn}^{2+}$  and  $\text{Nb}^{5+}$  cations and show promising ferroelectric and piezoelectric properties <sup>23-33</sup>. Similar to (1-x)BZT-xPT,  $(1-x)\text{Bi}(\text{Zn}_{2/3}\text{Nb}_{1/3})\text{O}_3-x\text{PbTiO}_3$  [(1-x)BZN-xPT] system demonstrates a highly tetragonally distorted crystal structure and a high  $T_C$  (e.g. tetragonality  $c/a \approx 1.08$  and

$T_C \approx 530$  °C for  $x = 0.8$  with  $c$  and  $a$  the lattice parameters of the unit cell) without showing MPB<sup>30, 34, 35</sup>. However, the coercive field ( $E_C$ ) of (1- $x$ )BZN- $x$ PT ceramics is too high to realize the domain switching, so no useful ferroelectric and piezoelectric properties could be found.

In the (1- $x$ )BZN- $x$ PT system, when  $\text{PbZrO}_3$ , one of the end members in PZT with orthorhombic crystal structure, is incorporated into (1- $x$ )BZN- $x$ PT tetragonal crystals to form a ternary solid solution, an MPB similar to that PZT can be formed and thus it is possible to design new piezoelectric materials with enhanced electromechanical properties and high  $T_C$ . Based on the abovementioned strategy, in this work, pseudo-binary (1- $x$ )[0.2Bi(Zn<sub>2/3</sub>Nb<sub>1/3</sub>)O<sub>3</sub>-0.8PbTiO<sub>3</sub>]- $x$ PbZrO<sub>3</sub> [(1- $x$ )BZNPT- $x$ PZ] solid solution ceramics are synthesized and their crystal structure, dielectric, ferroelectric and piezoelectric properties are studied systematically. Phase transformation sequences of tetragonal  $\rightarrow$  rhombohedral  $\rightarrow$  orthorhombic with a PZT-like MPB and favorable electrical properties are realized in ceramics of (1- $x$ )BZNPT- $x$ PZ solid solution, thereby providing a new family of ferroelectric and piezoelectric materials potentially useful for high performance electromechanical transducer applications.

## Experimental Procedures

The (1- $x$ )[0.2Bi(Zn<sub>2/3</sub>Nb<sub>1/3</sub>)O<sub>3</sub>-0.8PbTiO<sub>3</sub>]- $x$ PbZrO<sub>3</sub> solid solutions in the full composition range ( $x = 0 - 1$ ) were synthesized using the traditional solid-state reaction method. Stoichiometric ratios of PbO, Bi<sub>2</sub>O<sub>3</sub>, ZnO, Nb<sub>2</sub>O<sub>5</sub>, ZrO<sub>2</sub> and TiO<sub>2</sub> powders (purity  $\geq 99.9$  %), with 2 mol% excess of Bi<sub>2</sub>O<sub>3</sub> and PbO to compensate for the volatilization of bismuth and lead oxides at high temperatures, were mixed and ground for 2 h by using an agate mortar and pestle. The mixture was then pressed and calcined at 850 - 900 °C for 6 h to form the perovskite phase. Then the calcinated powders were ball-milled in ethanol with zirconia balls in sealed plastic jars for 12 h. 5 wt% polyvinyl acetate (PVA) binder was then added to dried powders and the obtained samples were pressed into round discs with the diameter of 10mm for sintering. After burning off the PVA binder at 600 °C, the pellets were sintered in the temperature range of 1100 °C -

1200 °C for 2 h to densify the ceramics. In order to suppress the evaporation of PbO and Bi<sub>2</sub>O<sub>3</sub> at high temperatures, the pellets were buried in a sacrificial powder of the same composition during sintering. Note that all the compositions mentioned in this work refer to the nominal compositions of the solid solution system.

The as-sintered ceramics were polished to have flat and parallel surfaces to perform X-ray diffraction (XRD) measurements. XRD measurements were carried out on a Rigaku Rapid-Axis Diffractometer at a rapid scanning rate ( $2\theta = 10 - 80^\circ$  for 15 minutes) and on a Bruker D8 Advance Diffractometer at a much slower scanning rate ( $2\theta = 36 - 46^\circ$  with step length = 0.02 °/step and speed = 2 s/step) for high-quality data collections for the structural refinement, which cover the (111)<sub>C</sub> and (200)<sub>C</sub> diffraction peaks. Both instruments used a Cu K $\alpha$  X-ray source. Pawley refinements were carried out to fit the peak shape of the diffraction patterns and to calculate the lattice parameters of the unit cell for each composition. The samples were mirror polished and annealed at 600 °C for 0.5 h before the piezoresponse force microscopy (PFM) measurements. The domain structures and their dynamics were investigated by PFM with a modified commercial atomic force microscopic system in piezoresponse mode (AFM, Dimension ICON, NanoScope V, Bruker). Selected area electron diffraction (SAED) patterns were obtained using a JEOL JEM-F200 (HR) field emission transmission electron microscope (TEM) at room temperature. The samples for the SAED experiments were prepared by grinding pellets in an agate mortar followed by scooping the small fragments onto glued copper grids.

The pellets were painted with silver paste and then fired at 550 °C for 30 min to achieve a good Ohmic contact for electrical measurements. The samples of different compositions were poled at room temperature under a static electric field of 30 - 180 kV/cm for 20 min. The piezoelectric coefficient,  $d_{33}$ , was measured using a quasi-static piezoelectric meter (Model ZJ-6B, Institute of Acoustics, Beijing, China) after poling. The impedance of these poled specimens was measured at room temperature to determine the resonance and anti-resonance frequencies and calculate the planar electromechanical coupling factor ( $k_p$ ). The temperature dependences of the dielectric constant and loss tangent of the poled and unpoled samples were measured at various

frequencies using a Novocontrol Alpha high-resolution broadband dielectric analyzer upon heating. The polarization-electric field  $P(E)$  hysteresis loops of the samples were measured by the Sawyer-Tower technique using a Radiant RT-66 standardized ferroelectric testing system at room temperature.

## Results and Discussion

### (a) Crystal Structure Analysis

The quality of the sintered ceramics was good as the shrinkage was  $>10\%$  in diameter. Figure 1 shows the room-temperature powder XRD patterns of the  $(1-x)\text{BZNPT}-x\text{PZ}$  ( $x = 0 - 1$ ). All the compositions crystallized in a perovskite structure, indicating the formation of a stable solid solution. For  $x = 0$  (pure  $0.2\text{BZN}-0.8\text{PT}$ ), a typical tetragonal symmetry with large  $c/a$  ratio (tetragonality  $\approx 1.073$ ) was found, which is comparable to the previously reported results<sup>30, 34, 35</sup>. With increasing PZ content, the (002) and (200) diffraction peaks move closer, indicating the decrease of the tetragonal distortion. For compositions with relatively high PZ content ( $x \geq 0.6$ ), the  $(200)_C$  peaks become single while the  $(111)_C$  peak splits, revealing a rhombohedral crystal structure. Therefore, an MPB can be expected in the  $(1-x)\text{BZNPT}-x\text{PZ}$  system between the tetragonal and rhombohedral phases. When  $x \geq 0.95$ , the crystal transforms into orthorhombic symmetry as seen from the superlattice peaks which are marked by the asterisks in Figure 1.

In order to confirm the existence of a MPB in the  $(1-x)\text{BZNPT}-x\text{PZ}$  system, high-resolution XRD data were collected between  $2\theta = 36 - 46^\circ$  to cover the  $(111)_C$  and  $(200)_C$  peaks for  $x = 0.3 - 0.6$  as shown in Figure 2. For  $x = 0.3$ , the  $(111)_C$  and  $(200)_C$  peaks were well fitted by a single peak and double peak pattern, respectively. Therefore, the crystal was confirmed to have a pure tetragonal phase for  $x = 0.3$ . In comparison, the XRD pattern for the composition  $x = 0.6$  was fitted to have a double  $(111)_C$  peak and a single  $(200)_C$  peak, which is suggestive of a pure rhombohedral phase. For the composition range of  $0.3 < x < 0.6$ , however, the XRD patterns fit with neither the pure

tetragonal phase nor the pure rhombohedral phase, indicating the coexistence of the two phases. For instance, for  $x = 0.4$ , a shoulder in the lower angle of the  $(111)_C$  peak and an additional peak between the  $(002)$  and  $(200)$  diffraction peaks were observed in its XRD pattern, which manifests a MPB with the mixture of tetragonal and rhombohedral phases. A similar peak profile was also observed for  $x = 0.5$ . These results confirm the existence of a broad MPB region in the composition range of  $0.4 \leq x \leq 0.5$ . Based on the aforementioned observations, a phase transition sequences of tetragonal  $\rightarrow$  MPB  $\rightarrow$  rhombohedral  $\rightarrow$  orthorhombic is present in the  $(1-x)\text{BZNPT}-x\text{PZ}$  system as the PZ concentration increases, which is akin to the well-known PZT system.

The lattice parameters of the  $(1-x)\text{BZNPT}-x\text{PZ}$  system at room temperature were calculated based on the Pawley refinements, as shown in Figure 3. To clearly demonstrate the variation of the lattice parameters with composition and to compare the obtained lattice parameters with those of PZT ceramics, the lattice parameters of the orthorhombic  $(1-x)\text{BZNPT}-x\text{PZ}$  and PZT crystals ( $Pbam$  space group with eight formula units) were converted into pseudo-tetragonal lattice parameters using the following equations:

$$\begin{aligned} a_{\text{pT}} = b_{\text{pT}} &= \frac{1}{2} \sqrt{a_{\text{O}}^2 + \left(\frac{b_{\text{O}}}{2}\right)^2} \\ c_{\text{pT}} &= \frac{1}{2} c_{\text{O}} \end{aligned} \quad (1)$$

where the subscript “pT” and “O” represent the pseudo-tetragonal unit cell and the orthorhombic unit cell, respectively. The unit cell volume ( $V$ ) of the orthorhombic crystal is  $V = a_{\text{O}}b_{\text{O}}c_{\text{O}}/8$ , which is almost the same as the value calculated by the tetragonal unit cell volume equation:  $V = (a_{\text{pT}})^2c_{\text{pT}}$ . It is clear that the volume of the crystal gradually increases with the increasing of PZ content. The increasing trend of the volume is due to the larger ionic radii of  $\text{Pb}^{2+}$  and  $\text{Zr}^{4+}$  than those of other cations [ $r(\text{Pb}^{2+}) = 1.49 \text{ \AA}$ ,  $r(\text{Bi}^{3+}) = 1.36 \text{ \AA}$ ,  $r(\text{Zr}^{4+}) = 0.72 \text{ \AA}$ ,  $r(\text{Nb}^{5+}) = 0.64 \text{ \AA}$ ,  $r(\text{Ti}^{4+}) = 0.605 \text{ \AA}$ ,  $r(\text{Zn}^{2+}) = 0.74 \text{ \AA}$ ], which expand the cell volume.

Based on the obtained lattice parameters, the  $c/a$  values (tetragonality of the unit cell) of the  $(1-x)\text{BZNPT}-x\text{PZ}$  solid solutions were calculated, as shown in Figure 4. For

comparison, the  $c/a$  values of the PZT system obtained from Jaffe *et al.*'s work<sup>11</sup> are also given in Figure 4. A large tetragonality ( $c/a \approx 1.08$ ), which is higher than that of PT ( $c/a \approx 1.06$ ), is observed for the 0.2BZN-0.8PT solid solution, indicating a very large tetragonal distortion in the (1- $x$ )BZN- $x$ PT system. As shown in Figure 4, with increasing PZ content, the  $c/a$  values show considerable decrease before dropping to 1 for the rhombohedral structure of both (1- $x$ )BZNPT- $x$ PZ and PZT. Compared with PZT, the tetragonality of (1- $x$ )BZNPT- $x$ PZ decrease more rapidly with the increase of PZ content and eventually becomes smaller than that of PZT at  $x > 0.1$ , indicating that the decrease of the tetragonal distortion with increasing PZ content would be further promoted due to the incorporation of BZN for PZ content  $x > 0.1$ .

For the compositions with the orthorhombic phase, the  $c/a$  ratio is calculated from  $c_{pT}/a_{pT}$ , which is smaller than 1, giving a flattened-cuboid-like unit cell. According to the Landau theory and related studies<sup>36-40</sup>, an empirical relationship  $T_C \propto P_S^2 \propto c/a - 1$  was found with  $T_C$ ,  $P_S$  and  $c/a$ , the Curie temperature, spontaneous polarization and tetragonality of a tetragonal crystal, respectively. As the tetragonality decreases rapidly with PZ concentration (Figure 4), we can predict that  $T_C$  and  $P_S$  will also decrease rapidly with the increase of PZ content in the (1- $x$ )BZNPT- $x$ PZ system.

## (b) Dielectric properties and phase transition characters

The temperature dependences of the dielectric constant ( $\epsilon$ ) and loss tangent ( $\tan\delta$ ) of the (1- $x$ )BZNPT- $x$ PZ ceramics were measured at various frequencies. Since no frequency dispersion was observed in the dielectric behavior of all the compositions, the temperature dependence of the dielectric constant measured at 100 kHz was shown as an example in Figure 5, from which we can determine the phase transition feature for different compositions. The temperature corresponding to the maximum of the dielectric constant,  $T_C$ , decreases gradually with increasing PZ content  $x$ . For the compositions within the MPB region ( $0.4 \leq x \leq 0.5$ ), an additional dielectric anomaly below  $T_C$  can be observed, which can be more clearly visualized in the temperature dependence of the first derivative of the dielectric constant and loss tangent versus

temperature, i. e.  $\frac{d\varepsilon(T,x,f)}{dT}$  and  $\frac{d}{dT}(\tan\delta(T,x,f))$ , respectively. More detailed explanations can be found in Ref. 28. Taking the composition  $x = 0.5$  as an example, the temperature (281 °C) at which  $\frac{d\varepsilon}{dT} = 0$  with  $\varepsilon$  reaching its maximum corresponds to  $T_C$ . Another dielectric anomaly is found at around 214 °C, where  $\frac{d}{dT}(\tan\delta)$  and  $\frac{d\varepsilon}{dT}$  correspondingly reach their extremums (Figure 6 (a)). This additional dielectric anomaly below  $T_C$  is generally believed to be the structural phase transition temperature at the MPB region (such as the rhombohedral to tetragonal phase transition temperature) and is usually marked as  $T_{\text{MPB}}$ <sup>11-14</sup>. It should be noted that the value of  $T_{\text{MPB}}$  (214 °C) in the newly developed (1-x)BZNPT-xPZ system is significantly higher than that of the pure PZT ceramics in the MPB region ( $T_{\text{MPB}} \approx 100$  °C for  $\text{Pb}(\text{Zr}_{0.52}\text{Ti}_{0.48})\text{O}_3$ )<sup>11</sup>.

For compositions with relatively high PZ content ( $0.6 \leq x \leq 0.9$ ) that demonstrate rhombohedral phase symmetry at room temperature, the dielectric anomaly below  $T_C$  was also observed [e.g. the temperature at  $\sim 97$  °C for  $x = 0.8$  as shown in the dielectric constant and dielectric loss features in Figure 6(b)].

As we know, for the PZ-rich PZT solid solution, there are two different rhombohedral phases in different temperature ranges. One is the ferroelectric rhombohedral phase with  $R3c$  space group [ $F_R(\text{LT})$ ] at low temperatures. In the  $F_R(\text{LT})$  phase, the antiphase oxygen octahedral tilting was found in the perovskite unit cell, which was denoted as  $a^-a^-a^-$  by Glazer *et al.*<sup>41, 42</sup>. The magnitude of the octahedral tilting gradually decreases with the increase of temperature and becomes zero in the high temperature rhombohedral phase with  $R3m$  space group [ $F_R(\text{HT})$ ], which can be denoted as  $a^0a^0a^0$ . Considering the similarities between the (1-x)BZNPT-xPZ and PZT systems, it is reasonable to believe that the dielectric anomaly at the low temperature range corresponds to the  $F_R(\text{LT})$  to  $F_R(\text{HT})$  phase transition. Due to the oxygen octahedral rotation in the  $R3c$  phase, there should be a  $(\frac{3}{2} \frac{1}{2} \frac{1}{2})_C$  superlattice reflection at around  $2\theta = 37^\circ$ . However, we did not observe this superlattice peak in our XRD patterns (Figure 1 and Figure 2), which might be due to the low scattering factor of oxygen for X-ray, making the reflection indiscernible.

The SAED on TEM is proved to be a viable method for identifying the octahedral tilts in perovskites. Figure 7 shows, as an example, the room-temperature electron diffraction patterns of the  $x = 0.7$  sample with zone axes chosen as (a)  $[100]_c$ , (b)  $[111]_c$ , (c)  $[0\bar{1}1]_c$  and (d)  $[011]_c$ , respectively. The  $(\frac{1}{2} \frac{1}{2} \frac{1}{2})_c$  superlattice reflection spots are present along the  $[0\bar{1}1]_c$  zone axes (Figure 7(c)), while no superlattice reflection is observed for the diffraction patterns along the  $[100]_c$ ,  $[111]_c$  and  $[011]_c$  zone axes. This results indicate the presence of an  $a^-a^-a^-$  octahedral tilt system (according to the Glazer notation) and the  $R3c$  space group at room temperature<sup>43-45</sup>. This octahedral tilt is believed to arise from the substitution of the antiferroelectric PZ. The observed octahedral tilt is believed to arise from the structural effects of the partial substitution of antiferroelectric PZ.

For the compositions with orthorhombic symmetry at room temperature ( $x = 0.95$ ), a dramatic increase of the dielectric constant and loss tangent could be found with increasing temperature before the dielectric anomaly at  $\sim 117$  °C, which, by analogy with the phase transition behavior in the PZT system<sup>11, 14, 15, 46</sup>, indicates an orthorhombic to rhombohedral phase transition.

Based on the above dielectric results and the crystal structure analysis, a composition-temperature phase diagram is established, as shown in Figure 8. For comparison, the most classic PZT phase diagram established by Jaffe *et al.*<sup>11</sup> is also shown. Evidently from Figure 8, the phase diagrams of the  $(1-x)\text{BZNPT}-x\text{PZ}$  and PZT systems share a lot of similarities, including the composition dependent phase transition from tetragonal to rhombohedral to orthorhombic phases with an MPB bridging as a mixture phase. The Curie temperature decreases nonlinearly with increasing PZ content, and in the MPB region, both of the  $T_{\text{MPB}}$  values increase with increase PZ content. The variation trend of  $T_C$  and  $T_{\text{MPB}}$  with regard to the composition in these two systems are typical phenomena for MPB-based solid solutions<sup>11, 47</sup>, giving rise to a curved MPB line in the phase diagram. By comparing the two systems, we can see that the MPB line in  $(1-x)\text{BZNPT}-x\text{PZ}$  is more curved than that of PZT, leading to a broader MPB region than that of PZT ( $x \approx 0.4$  to  $0.5$  for  $(1-x)\text{BZNPT}-x\text{PZ}$  and  $x \approx 0.52$  to  $0.55$  for PZT<sup>9-15</sup>).

Consequently, enhanced piezo-/ferroelectric performances can be obtained within a wider composition range in  $(1-x)\text{BZNPT}-x\text{PZ}$  than in PZT.

The broadening of the MPB in the  $(1-x)\text{BZNPT}-x\text{PZ}$  system could be explained by the gradually disordered distribution of the ions at the equivalent crystallographic positions due to the incorporation of BZN, which gives rise to an enhanced nanoscale inhomogeneity and therefore suppresses the composition-driven (different  $\text{Zr}^{4+}$  concentration) structure change<sup>28</sup>. Comparing the  $T_C$  of the  $(1-x)\text{BZNPT}-x\text{PZ}$  system with that of the PZT system for the same PZ content (Figure 8), the former has a lower  $T_C$  for most compositions than the latter, except for  $0.2\text{BZN}-0.8\text{PT}$  ( $x = 0$ ) that exhibits a higher  $T_C = 530\text{ }^\circ\text{C}$  than that of pure PT ( $T_C = 490\text{ }^\circ\text{C}$ ). The  $T_C$  values decrease more rapidly in the tetragonal region than in the rhombohedral region for the  $(1-x)\text{BZNPT}-x\text{PZ}$  system with the addition of PZ content; however, in the PZT system, the  $T_C$  values show a slower decreasing trend in the tetragonal region than in the rhombohedral region. In many perovskite ferroelectrics, the Curie temperature is found to be proportional to the extent of the crystal distortion caused by the coupling effect between different cations<sup>39, 48, 49</sup>. Therefore, with the increase of PZ content, the more rapid decrease of  $T_C$  in  $(1-x)\text{BZNPT}-x\text{PZ}$  than that in PZT in the tetragonal phase indicates that the incorporation of PZ results in more prominent change of distortion in the crystalline lattice of  $(1-x)\text{BZNPT}-x\text{PZ}$  than in the crystalline lattice of PZT, which is in agreement with the crystal structure analysis (Figure 3 and Figure 4).

### (c) Ferroelectric and piezoelectric properties

Figure 9 (a)-(e) shows the polarization-electric field  $P(E)$  hysteresis loops of  $(1-x)\text{BZNPT}-x\text{PZ}$  ceramics with selected compositions at room temperature and 10 Hz. Most of the samples exhibit saturated  $P(E)$  hysteresis loops, indicating good ferroelectric properties. For  $x = 0$  (Figure 9 (a)), the  $P(E)$  hysteresis loops did not reach saturation until dielectric breakdown occurred at 180 kV/cm, suggesting the high coercive electric field beyond the dielectric breakdown field. A similar result was obtained for  $x = 0.1$  with a very small remnant polarization ( $P_r$ ). As the PZ content is

further increased, saturated  $P(E)$  hysteresis loops could be observed and the coercive field gradually decreases as shown in Figure 9 (b) - (d) and (f). The decrease of  $E_C$  with the increase of PZ content is related to the decreasing crystal distortion as shown in Figure 4. The remnant polarization,  $P_r$ , reaches its maximum ( $P_r = 31.2 \mu\text{C}/\text{cm}^2$ ) at  $x = 0.5$ , which is located at the MPB region. The highest  $P_r$  value achieved in the MPB region is due to the multi-phase coexistence (rhombohedral and tetragonal phases) that leads to a synergetic effect of equivalent polarization states (such as eight equivalent (111) spontaneous polarization directions for the rhombohedral phase and six equivalent (001) directions for the tetragonal phase) in this system. As the PZ content is further increased ( $x \geq 0.95$ ), an orthorhombic antiferroelectric phase can be observed at room temperature. Under an electric field of  $\pm 60 \text{ kV}/\text{cm}$ , only a linear  $P(E)$  behavior is observed as shown in Figure 9 (e), suggesting that the critical field required to realize the antiferroelectric polarization switching is higher than  $60 \text{ kV}/\text{cm}$ .

The piezoelectric coefficient,  $d_{33}$ , and the planar electromechanical coupling factor,  $k_p$ , of the samples for different compositions were measured after the samples were poled under an electric field in the range of  $30 - 180 \text{ kV}/\text{cm}$  for 20 min at room temperature. After the samples were aged at room temperature for 24 h, the  $d_{33}$  value and the resonance and anti-resonance frequencies were recorded. The measured  $d_{33}$  and calculated  $k_p$  values are listed in Table 1. For compositions of  $x = 0$  and  $0.1$ , very weak piezoelectric responses were detected ( $d_{33} \leq 3 \text{ pC}/\text{N}$ ). The lower achievable  $d_{33}$  value is due to the fact that the coercive field of these samples is too high to allow them to be completely poled before they break down. The  $d_{33}$  and  $k_p$  values gradually increase and then decrease with increasing PZ content. Optimal  $d_{33}$  and  $k_p$  values were found to be  $260 \text{ pC}/\text{N}$  and  $0.41$ , respectively, at the composition of  $x = 0.5$ , which is in the MPB region. The obtained  $d_{33}$  value is higher than that of the pure PZT ceramics ( $\approx 200 \text{ pC}/\text{N}$ )<sup>11</sup>. According to the phenomenological free energy theory<sup>16, 17, 50</sup>, the flattened free energy as a function of polarization for the compositions in MPB region facilitates the polarization rotation. Microscopically, the stereochemically active lone pair electrons on  $\text{Bi}^{3+}$  and the ferroelectrically active  $\text{Zn}^{2+}$  and  $\text{Nb}^{5+}$  ions enlarge the local crystal distortion and thereby inherently enhance the piezoelectric properties<sup>49</sup>. For

compositions  $x = 0.95$  and 1, no piezoelectric response was detected because the crystal has a nonpolar antiferroelectric phase at room temperature.

#### **(d) Local polar structure and the origin of the high piezoelectricity near the MPB region**

Piezoresponse force microscopy provides nanoscale insights into the polar domain structure and polarization switching, which helps to better understand the electromechanical behaviour in ferroelectric materials<sup>51-55</sup>. Figure 10 (a)-(d) shows the out-of-plane (OP) amplitude and phase images of the (a)  $x = 0.3$ , (b)  $x = 0.4$ , (c)  $x = 0.5$  and (d)  $x = 0.6$  ceramics, respectively, whose compositions cross the MPB region in the  $(1-x)\text{BZNPT}-x\text{PZ}$  solid solution. (The in-plane PFM images show similar characters to the out-of-plane ones because of the randomly oriented polarizations in the polycrystalline ceramics. Therefore, the in-plane images are not given here.) The square-shaped images were obtained in a  $10.0\ \mu\text{m} \times 10.0\ \mu\text{m}$  area in each sample, which covered several grains of the ceramics. As revealed by the OP amplitude and phase images in Figure 10, all the samples exhibit very complex domain configurations. The domain size varies from dozens of nanometers to micrometer for each sample. No significant change of the domain size was found for the different compositions. However, the OP amplitude, which reflects the piezoresponse, i.e.  $d_{33}$ , differs a lot among the four samples. The OP amplitude of the MPB compositions ( $x = 0.4$  and  $x = 0.5$ ) is significantly higher than that of the rhombohedral and tetragonal compositions. The high piezoresponse is even more prominent for  $x = 0.5$  as indicated by the larger blue areas observed in the OP amplitude image (Figure 10(c)).

It is well known that the piezoelectric activity typically includes two contributions, i.e., intrinsic and extrinsic. The intrinsic contribution is related to the linear lattice distortion, which is associated with the change in the polarization of the unit cell. The extrinsic contributions refer to other responses different from the intrinsic one, such as the non- $180^\circ$  domain wall and interphase boundary motions<sup>56-59</sup>. Without applying an electric field, the measured piezoresponse amplitude mainly reflects the intrinsic

contributions because the driving voltage for the PFM measurement is too small to induce significant domain change (domain wall motion). The larger amplitude obtained in  $x = 0.5$  (Figure 10(c)) indicates a greater contribution from the intrinsic piezoresponse. These results are expected as the small-signal piezoelectric coefficient  $d_{33}$  reaches maximum values at the same composition (See Table 1). The measured results clearly reveal that the lattice distortion is significantly enhanced in the MPB region of the  $(1-x)\text{BZNPT}-x\text{PZ}$  solid solutions. The large intrinsic piezoresponse in the MPB region is believed to arise from the flattening of the free energy barrier, which facilitates the polarization rotation<sup>16-18, 50</sup>.

In addition to the intrinsic contribution, the extrinsic contributions also account for the total piezoelectric response. The domain dynamics is investigated to give some hints on the extrinsic contributions in the  $(1-x)\text{BZNPT}-x\text{PZ}$  solid solutions. The PFM measurements were performed after the sample was poled (with a rectangle area of  $3.3 \mu\text{m} \times 10.0 \mu\text{m}$  in the center part of the area where the first PFM measurements were performed). By applying a voltage along the out-of-plane direction, the polarization was gradually reoriented and aligned generally along the out-of-plane direction under 40 V, as shown in Figure 10 (where the contrast in the phase images indicates the polarization direction). It is interesting to note that it is more difficult to realize the polarization switching in the MPB compositions ( $x = 0.4$  and  $x = 0.5$ ) than in the tetragonal ( $x = 0.3$ ) and rhombohedral ( $x = 0.6$ ) crystals. This phenomenon becomes more distinct in the reverse switching process by applying a negative voltage, where a poling voltage of -40 V is not sufficient to switch the polarization completely for  $x = 0.5$ . Due to the random orientation of the grains, the  $180^\circ$  and non- $180^\circ$  domain switching cannot be distinguished in polycrystalline ceramics by PFM measurements. However, compared with non- $180^\circ$  domains, the  $180^\circ$  domains will not induce additional strain and hence should be easier to switch in a crystal with a certain symmetry<sup>60</sup>. This result suggests that the (non- $180^\circ$ ) domain switching might be clamped in the MPB compositions of  $(1-x)\text{BZNPT}-x\text{PZ}$ , which would not be favourable for high piezoelectricity. To fully clarify the origin of domain clamping in the MPB compositions, further experimental and theoretical studies are required.

To verify the stability of the ferroelectric domains, long-time relaxation PFM measurements were conducted after each sample was poled under -40 V for 2 h. No significant change was found, indicating good stability of the domains, which further reveals the weak domain mobility in the samples.

The above-mentioned results clearly indicate that the intrinsic and extrinsic piezoelectric contributions do not necessarily follow the same trend. From this observation, we believe that the intrinsic contribution, i.e., the crystallographic nature of the lattice is the dominant factor leading to the high piezoelectric activity in the MPB region of the  $(1-x)\text{BZNPT}-x\text{PZ}$  solid solutions.

#### **(d) Antiferroelectric and ferroelectric phase stability**

As found in this work, a sequence of phases appears in the  $(1-x)\text{BZNPT}-x\text{PZ}$  solid solutions with increasing  $x$ , from a ferroelectric tetragonal phase to a ferroelectric rhombohedral phase with a morphotropic phase boundary in between, and finally to an orthorhombic antiferroelectric phase. The chemical and structural origin of such a phase transition sequence is worth being discussed. From the structural point of view, ferroelectric  $0.2\text{Bi}(\text{Zn}_{2/3}\text{Nb}_{1/3})\text{O}_3-0.8\text{PbTiO}_3$  has a tetragonal symmetry with an ultralarge off-center displacement of the B-site cations ( $\text{Zn}^{2+}/\text{Nb}^{5+}/\text{Ti}^{4+}$ ) along the  $c$ -axis (Figure 11(a)), which is the origin of its strong ferroelectricity at room temperature (and its high  $T_C$ )<sup>26, 30</sup>. In comparison,  $\text{PbZrO}_3$  has an orthorhombic antiferroelectric phase at room temperature, the antiferroelectricity of which originates from the antiparallel displacement of  $\text{Pb}^{2+}$  along the pseudocubic  $[110]_C$  directions (Figure 11(b)). Due to the different local environments of the cations in the two end members, strong competition between ferroelectric order and antiferroelectric ordering exists, which could lead to dipole frustration and possibly incommensurate modulation in the  $(1-x)\text{BZNPT}-x\text{PZ}$  solid solutions<sup>61, 62</sup>.

From the soft-mode theory, the ferroelectric and antiferroelectric phase transitions result from the soft mode instabilities at the Brillouin zone center and Brillouin zone boundary, respectively, and the soft mode instability at a general point of the Brillouin

zone would lead to incommensurate domain structures. The instability causes the vibration frequency to decrease down to zero when the phase transition occurs. The occurrence of the phase transition is determined by the competition of the two phases, in which the long-range Coulomb force favours the ferroelectric phase, while the short-range force favours the antiferroelectric phase<sup>63-65</sup>.

Phenomenologically, the free energy of a ferroelectric ( $G_1$ ) can be described by the following equation based on the Landau-Devonshire theory<sup>5</sup>,

$$G_1 = a_1P^2 + b_1P^4 + c_1P^6, \quad (2)$$

where  $P$  is polarization and  $a_1$ ,  $b_1$  and  $c_1$  are temperature- and composition-dependent Landau coefficients. For ferroelectric state, the parameter  $c_1$  is positive and  $a_1$  is negative, giving rise to a double-minimum curve with minima at non-zero values of polarization (Figure 11 (c)).

In antiferroelectric materials, the free energy  $G_2$  can be expressed by the following equation considering the antipolar configuration of the two sublattice polarizations,

$$G_2 = a_2(P_1^2 + P_2^2) + b_2P_1^2P_2^2 + c_2(P_1^4 + P_2^4) + d_2(P_1^6 + P_2^6) - (P_a - P_b)E, \quad (3)$$

where  $P_1$  and  $P_2$  are the polarizations of two sublattices,  $E$  is the electric field, and  $a_2$ ,  $b_2$ ,  $c_2$ , and  $d_2$  are phenomenological parameters, which are also temperature- and composition-dependent. Here  $b_2 > 0$  is required to ensure the antipolar alignment of the two sublattices<sup>5, 66, 67</sup>. In the case of  $\text{PbZrO}_3$  at room temperature, the free energy of the antiferroelectric state is the lower than the metastable ferroelectric state, indicating that the antiferroelectric state is more stable. Nevertheless, the energy difference between the antiferroelectric and ferroelectric states is small due to the competition between two possible ordering states, as shown in Figure 11(d). Therefore, phase transition could occur between different phases with the change of external conditions such as temperature, external electric fields and composition.

When a solid solution is formed between a ferroelectric like  $0.2\text{Bi}(\text{Zn}_{2/3}\text{Nb}_{1/3})\text{O}_3$ - $0.8\text{PbTiO}_3$  and an antiferroelectric like  $\text{PbZrO}_3$ , the total energy equals to the linear combination of the energy of each component<sup>5</sup>. Therefore, additional energy minimum

is likely to be present, which determines the ordering state of the solid solution.

## Conclusions

A novel complex perovskite solid solution of  $(1-x)[0.2\text{Bi}(\text{Zn}_{2/3}\text{Nb}_{1/3})\text{O}_3-0.8\text{PbTiO}_3]-x\text{PbZrO}_3$  ( $x = 0 - 1$ ) was prepared in the form of ceramics by the solid-state reaction method. The  $0.2\text{Bi}(\text{Zn}_{2/3}\text{Nb}_{1/3})\text{O}_3-0.8\text{PbTiO}_3$  system was chemically modified by the incorporation of antiferroelectric  $\text{PbZrO}_3$  (PZ). The crystal structure, electrical properties including dielectric, ferroelectric and piezoelectric properties, and phase transition characters were studied in detail. Crystal structure analysis indicated the phase transformation sequences of tetragonal  $\rightarrow$  rhombohedral  $\rightarrow$  orthorhombic with a PZT-like MPB in the new  $\text{Bi}(\text{Zn}_{2/3}\text{Nb}_{1/3})\text{O}_3-\text{PbTiO}_3-\text{PbZrO}_3$  ternary system. The incorporation of BZN into PZT broadens the MPB composition range compared with pure PZT, leading to a significantly curved MPB in the phase diagram. The phase transition temperatures, including ferroelectric to paraelectric phase transition temperature ( $T_C$ ), rhombohedral to tetragonal phase transition temperature at the MPB ( $T_{\text{MPB}}$ ), antiferroelectric to ferroelectric phase transition temperature ( $T_{\text{AF-F}}$ ) and the low temperature to high temperature phase transition temperature in the rhombohedral crystal ( $T_{\text{FRLT-FRHT}}$ ), of various compositions were determined from the dielectric measurements, and a temperature-composition phase diagram of the  $(1-x)\text{BZNPT}-x\text{PZ}$  system was successfully established. Attractive electrical properties were obtained in the MPB composition range ( $d_{33} = 260$  pC/N,  $k_p = 0.41$ ,  $P_r = 31.2$   $\mu\text{C}/\text{cm}^2$ ,  $E_C = 16$  kV/cm,  $T_C = 281$   $^\circ\text{C}$  and  $T_{\text{MPB}} = 214$   $^\circ\text{C}$  for  $x = 0.5$ ). The high piezoelectric properties obtained in the MPB composition was determined to arise from the significantly enhanced intrinsic contribution as evidenced by the piezoresponse force microscopy investigation. These impressive piezoelectric properties with a high  $T_C$  and in particular a high  $T_{\text{MPB}}$  arise from the MPB, which accommodates coexisting phases that facilitate the polarization rotations. Furthermore, the unique crystal chemistry of this system: the stereochemically active lone pair of electrons on  $\text{Bi}^{3+}$  and the ferroelectrically active  $\text{Zn}^{2+}$  and  $\text{Nb}^{5+}$  ions enlarges the local crystal distortion and thereby inherently enhances

the piezoelectric properties. The obtained properties in the MPB compositions make this system an interesting material for potential advanced electromechanical applications. This work could help to understand the origin of the high piezoelectricity in bismuth-based solid solutions and opens up further investigation into other bismuth-based solid solutions with an MPB that could exhibit higher piezo-/ferroelectric performance.

## Acknowledgments

The authors would like to thank Dr. Jinyan Zhao for the helpful discussion on the PFM results and Dr. Chao Li at the Instrument Analysis Center of Xi'an Jiaotong University for his assistance with the SAED experiments. This work was supported by the Natural Science Foundation of China (Grant No. 51902244), the China Postdoctoral Science Foundation (Grant No. 2018M643632), the Natural Science Foundation of Shaanxi Province (Grant No. 2019JQ-389), the U. S. Office of Naval Research (Grants No. N00014-12-1-1045 and N00014-16-1-3106), the Natural Sciences and Engineering Research Council of Canada (NSERC, Grant No. 203773), and the “111 Project” of China (Grant No. B14040). ZL would like to acknowledge the China Scholarship Council (CSC) for supporting his studies at SFU.

## Author Contributions

Zuo-Guang Ye, Zenghui Liu, Hua Wu and Wei Ren developed and planned the original project. Zenghui Liu, Zeng Luo, Pan Gao and Hongyan Wan performed the experiments. Zenghui Liu drafted the first manuscript. All authors reviewed the manuscript.

## References

1. Ye, Z.-G., *Handbook of advanced dielectric, piezoelectric and ferroelectric materials: Synthesis, properties and applications*. Woodhead Publishing: Cambridge,

- U.K., 2008.
2. Manjón-Sanz, A. M.; Dolgos, M. R., *Chem. Mater.* **2018**, *30* (24), 8718-8726.
  3. Wei, H.; Wang, H.; Xia, Y.; Cui, D.; Shi, Y.; Dong, M.; Liu, C.; Ding, T.; Zhang, J.; Ma, Y.; Wang, N.; Wang, Z.; Sun, Y.; Wei, R.; Guo, Z., *J. Mater. Chem. C* **2018**, *6* (46), 12446-12467.
  4. Zhang, S.; Li, F.; Jiang, X.; Kim, J.; Luo, J.; Geng, X., *Prog. Mater. Sci.* **2015**, *68*, 1-66.
  5. Uchino, K., *Ferroelectric Devices (2nd Edition)*. Marcel Dekker, Inc: New York, 2000.
  6. Xu, Y., *Ferroelectric materials and their applications*. North-Holland: New York, 1991.
  7. Li, F.; Cabral, M. J.; Xu, B.; Cheng, Z.; Dickey, E. C.; LeBeau, J. M.; Wang, J.; Luo, J.; Taylor, S.; Hackenberger, W.; Bellaiche, L.; Xu, Z.; Chen, L.-Q.; ShROUT, T. R.; Zhang, S., *Science* **2019**, *364* (6437), 264-268.
  8. Mitchell, R. H., *Perovskites: Modern and Ancient*. Almaz Press: Thunder Bay, ON, 2002.
  9. Haertling, G. H., *J. Am. Ceram. Soc.* **1999**, *82* (4), 796-818.
  10. Jaffe, B.; Roth, R. S.; Marzullo, S., *J. Appl. Phys.* **1954**, *25* (6), 809-810.
  11. Jaffe, B.; William, C.; Jaffe, H., *Piezoelectric ceramics*. Academic Press: London, 1971.
  12. Noheda, B.; Cox, D.; Shirane, G.; Guo, R.; Jones, B.; Cross, L., *Phys. Rev. B* **2000**, *63* (1), 014103.
  13. Noheda, B.; Cox, D. E.; Shirane, G.; Gonzalo, J. A.; Cross, L. E.; Park, S.-E., *Appl. Phys. Lett.* **1999**, *74* (14), 2059-2061.
  14. Zhang, N.; Yokota, H.; Glazer, A.; Ren, Z.; Keen, D.; Keeble, D.; Thomas, P.; Ye, Z.-G., *Nat. Commun.* **2014**, *5*, 5231.
  15. Zhang, N.; Yokota, H.; Glazer, A. M.; Thomas, P. A., *Acta Crystallogr. B* **2011**, *67* (5), 386-398.
  16. Fu, H.; Cohen, R. E., *Nature* **2000**, *403* (6767), 281-283.
  17. Guo, R.; Cross, L.; Park, S.; Noheda, B.; Cox, D.; Shirane, G., *Phys. Rev. Lett.* **2000**, *84* (23), 5423.
  18. Zhang, N.; Yokota, H.; Glazer, A. M.; Keen, D. A.; Gorfman, S.; Thomas, P. A.; Ren, W.; Ye, Z.-G., *IUCrJ* **2018**, *5*, 73-81.
  19. Zhang, S.; Yu, F., *J. Am. Ceram. Soc.* **2011**, *94* (10), 3153-3170.
  20. Richard, E. E.; Clive, A. R.; Thomas, R. S.; Paul, W. R.; Wes, H.; Seung-Eek, P., *Jpn. J. Appl. Phys.* **2001**, *40* (10R), 5999.
  21. Suchomel, M. R.; Davies, P. K., *Appl. Phys. Lett.* **2005**, *86* (26), 262905.
  22. Sehrioglu, A.; Sayir, A.; Dynys, F.; Nittala, K.; Jones, J., *J. Am. Ceram. Soc.* **2011**, *94* (3), 788-795.
  23. Paterson, A.; Wong, H. T.; Liu, Z.; Ren, W.; Ye, Z.-G., *Ceram. Int.* **2015**, *41*, S57-S62.
  24. Liu, Z.; Wu, H.; Paterson, A.; Ren, W.; Ye, Z.-G., *IEEE. T. Ultrason. Ferr.* **2017**, *64* (10), 1608-1616.
  25. Liu, Z.; Paterson, A.; Wu, H.; Gao, P.; Ren, W.; Ye, Z.-G., *J. Mater. Chem. C* **2017**,

- 5 (16), 3916-3923.
26. Liu, Z.; Wu, H.; Paterson, A.; Luo, Z.; Ren, W.; Ye, Z.-G., *Acta Mater.* **2017**, *136*, 32-38.
27. Liu, Z.; Wu, H.; Ren, W.; Ye, Z.-G., *Acta Mater.* **2018**, *149*, 132-141.
28. Liu, Z.; Gao, P.; Wu, H.; Ren, W.; Ye, Z. G., *Phys. Status. Solidi. A* **2018**, *215* (20), 1701007.
29. Paterson, A. R.; Zhao, J.; Liu, Z.; Wu, X.; Ren, W.; Ye, Z. G., *J. Cryst. Growth* **2018**, *486*, 38-44.
30. Paterson, A. R.-L. Crystal chemistry and properties of bismuth-modified complex oxide perovskites. Science: Department of Chemistry, 2017.
31. Liu, Z.; Luo, Z.; Wang, C.; Wu, H.; Zhang, N.; Liu, H.; Ren, W.; Ye, Z.-G., *Ceram. Int.* **2018**, *44*, S189-S194.
32. Liu, Z.; Yuan, Y.; Jaimeewong, P.; Wu, H.; Ren, W.; Ye, Z.-G., *Ferroelectrics* **2018**, *534* (1), 42-49.
33. Liu, Z.; Wu, H.; Ren, W.; Ye, Z.-G., *Ferroelectrics* **2018**, *533* (1), 183-191.
34. Nomura, S.; Kaneta, K.; Kuwata, J.; Uchino, K., *Mater. Res. Bull.* **1982**, *17* (12), 1471-1475.
35. Stringer, C. J.; Shrout, T. R.; Randall, C. A.; Reaney, I. M., *J. Appl. Phys.* **2006**, *99* (2), 024106.
36. Burns, G.; Scott, B. A., *Phys. Rev. B* **1973**, *7* (7), 3088.
37. Abrahams, S.; Kurtz, S.; Jamieson, P., *Phys. Rev.* **1968**, *172* (2), 551.
38. Zhang, X.; Kwon, D.; Kim, B. G., *Appl. Phys. Lett.* **2008**, *92* (8), 082906.
39. Chen, J.; Nittala, K.; Jones, J. L.; Hu, P.; Xing, X., *Appl. Phys. Lett.* **2010**, *96* (25), 252908.
40. Qi, T.; Grinberg, I.; Rappe, A. M., *Phys. Rev. B* **2010**, *82* (13), 134113.
41. Glazer, A., *Acta Crystallogr. B* **1972**, *28* (11), 3384-3392.
42. Glazer, A. M., *Acta Crystallogr. A* **1975**, *A31*, 756-762.
43. Ricote, J.; Corker, D. L.; Whatmore, R. W.; Impey, S. A.; Glazer, A. M.; Dec, J.; Roleder, K., *J. Phys.: Condens. Matter* **1998**, *10* (8), 1767-1786.
44. Woodward, D. I.; Reaney, I. M., *Acta Crystallogr. B* **2010**, *61* (4), 387-399.
45. Woodward, D. I.; Reaney, I. M.; Knudsen, J., *Phys. Rev. B* **2005**, *72* (10), 4110.
46. Barnett, H. M., *J. Appl. Phys.* **1962**, *33* (4), 1606-1606.
47. Noheda, B.; Cox, D.; Shirane, G.; Gao, J.; Ye, Z.-G., *Phys. Rev. B* **2002**, *66* (5), 054104.
48. Isupov, V., *Phys. Status. Solidi. A* **2000**, *181* (1), 211-218.
49. Grinberg, I.; Rappe, A., *Phys. Rev. Lett.* **2007**, *98* (3), 037603.
50. Damjanovic, D., *Appl. Phys. Lett.* **2010**, *97* (6), 062906.
51. Dittmer, R.; Jo, W.; Rödel, J.; Kalinin, S.; Balke, N., *Adv. Funct. Mater.* **2012**, *22* (20), 4208-4215.
52. Balke, N.; Bdikin, I.; Kalinin, S. V.; Kholkin, A. L., *J. Am. Ceram. Soc.* **2009**, *92* (8), 1629-1647.
53. Bonnell, D. A.; Kalinin, S. V.; Kholkin, A.; Gruverman, A., *MRS Bull.* **2009**, *34* (09), 648-657.
54. Gruverman, A.; Kalinin, S. V., *J. Mater. Sci.* **2006**, *41* (1), 107-116.

55. Vasudevan, R. K.; Balke, N.; Maksymovych, P.; Jesse, S.; Kalinin, S. V., *Appl. Phys. Rev.* **2017**, *4* (2), 051606-959.
56. Fancher, C. M.; Brewer, S.; Chung, C. C.; Röhrig, S.; Rojac, T.; Esteves, G.; Deluca, M.; Bassiri-Gharb, N.; Jones, J. L., *Acta Mater.* **2017**, *126*, 36-43.
57. Jones, J. L.; Aksel, E.; Tutuncu, G.; Usher, T.-M.; Chen, J.; Xing, X.; Studer, A. J., *Phys. Rev. B* **2012**, *86* (2), 024104.
58. Zhao, C.; Hou, D.; Chung, C.-C.; Zhou, H.; Kynast, A.; Hennig, E.; Liu, W.; Li, S.; Jones, J. L., *Acta Mater.* **2018**, *158*, 369-380.
59. Qiu, C.; Wang, B.; Zhang, N.; Zhang, S.; Liu, J.; Walker, D.; Wang, Y.; Tian, H.; Shrout, T. R.; Xu, Z.; Chen, L.-Q.; Li, F., *Nature* **2020**, *577* (7790), 350-354.
60. Cao, W., *Nat. Mater.* **2005**, *4* (10), 727.
61. Viehland, D.; Dai, X. H.; Li, J. F.; Xu, Z., *J. Appl. Phys.* **1998**, *84* (1), 458-471.
62. Gao, P.; Liu, Z.; Zhang, N.; Wu, H.; Bokov, A. A.; Ren, W.; Ye, Z.-G., *Chem. Mater.* **2019**, *31* (3), 979-990.
63. Hlinka, J.; Ostapchuk, T.; Buixaderas, E.; Kadlec, C.; Kuzel, P.; Gregora, I.; Kroupa, J.; Savinov, M.; Klic, A.; Drahoukoupil, J., *Phys. Rev. Lett.* **2014**, *112* (19), 197601.
64. Blinc, R., *Ferroelectrics* **1987**, *74* (1), 301-303.
65. Tagantsev, A.; Vaideeswaran, K.; Vakhrushev, S.; Filimonov, A.; Burkovsky, R.; Shaganov, A.; Andronikova, D.; Rudskoy, A.; Baron, A.; Uchiyama, H., *Nat. Commun.* **2013**, *4*.
66. Kittel, C., *Phys. Rev.* **1951**, *82* (5), 729.
67. Rabe, K. M., *Functional Metal Oxides* **2013**, 221-244.

Table 1: Piezoelectric coefficient  $d_{33}$  and planar mode electromechanical coupling factor  $k_p$  of the (1-x)BZNPT-xPZ ceramics .

$x$	0	0.1	0.2	0.3	0.4	0.5	0.6	0.7	0.8	0.9	0.95	1
$d_{33}$ (pC/N)	1	3	57	92	203	260	121	103	83	82	0	0
$k_p$	/	/	0.25	0.26	0.38	0.41	0.29	0.24	0.21	0.15	/	/

## Table of Content



Novel ferro-/piezoelectric solid solutions between bismuth-based perovskites and antiferroelectric materials are designed. Their crystal structure, phase transition, ferro-/piezoelectric properties and local polar structure are investigated in detail.

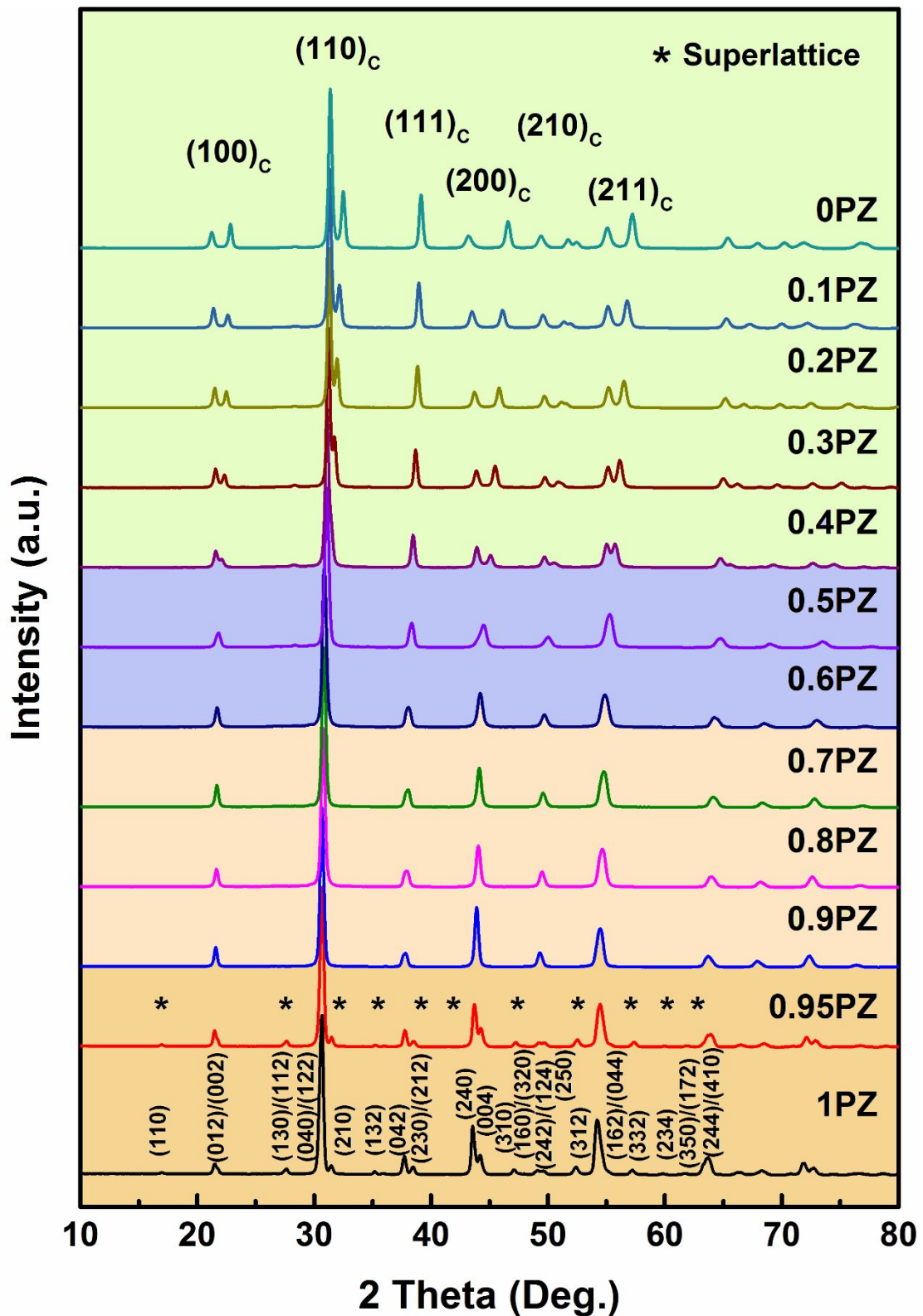


Figure 1. X-ray diffraction patterns of the  $(1-x)\text{BZNPT}-x\text{PZ}$  ceramics.

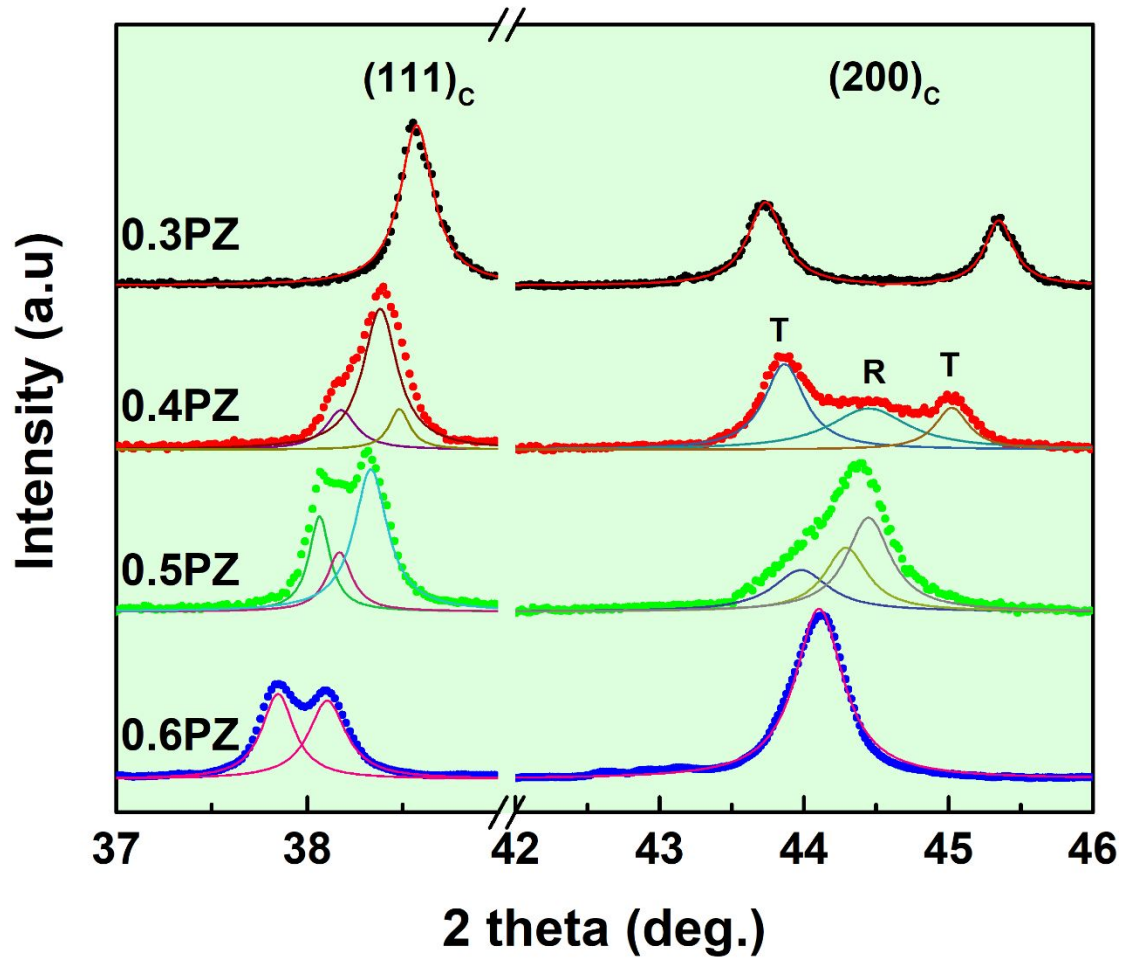


Figure 2. Detailed  $(111)_c$  and  $(200)_c$  peak profiles in the XRD patterns of the  $(1-x)\text{BZNPT}-x\text{PZ}$  ( $x = 0.3 - 0.6$ ) ceramics.

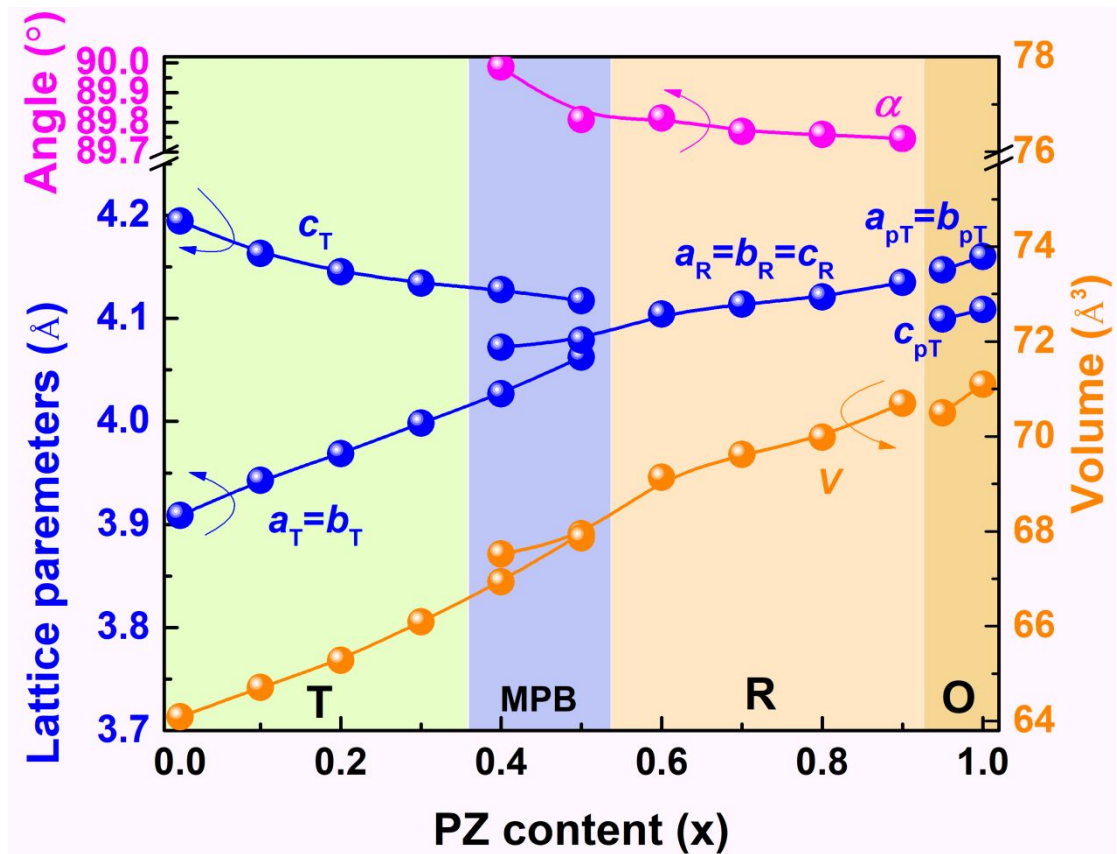


Figure 3. Variations of the room-temperature lattice parameters as a function of PZ content for the (1-x)BZNPT-xPZ solid solution. The lattice parameters ( $a_0$ ,  $b_0$  and  $c_0$ ) are converted into a pseudo-tetragonal setting and the volume of unit cell is calculated by  $V = a_0 b_0 c_0 / 8$  in the orthorhombic phase composition. See the text for details.

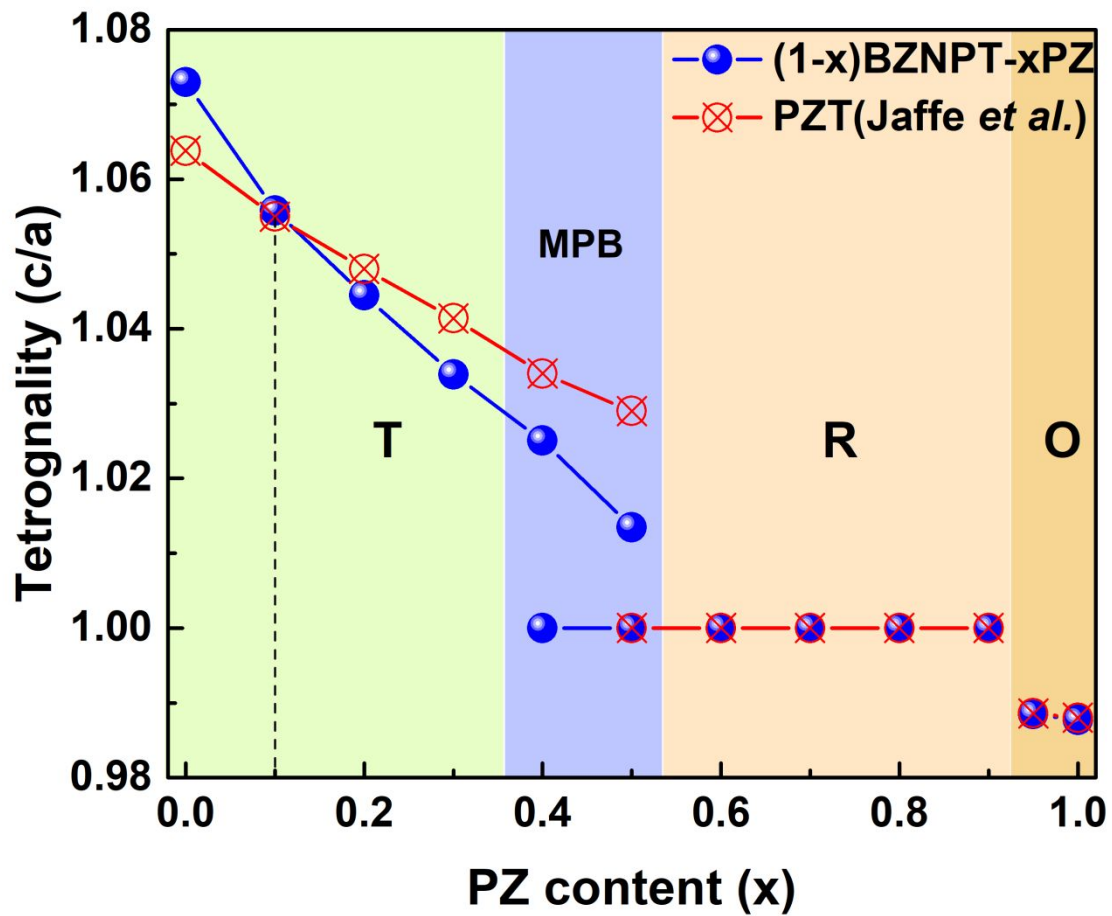


Figure 4. Variations of the tetragonality ( $c/a$ ) of the crystal unit cell as a function of PZ content for the  $(1-x)\text{BZNPT}-x\text{PZ}$  solid solution. For comparison, the  $c/a$  values of PZT obtained by Jaffe *et al.* are also presented<sup>11</sup>. In the orthorhombic phase composition, the  $c/a$  values are calculated from  $c_{pT}/a_{pT}$ . See the text for details.

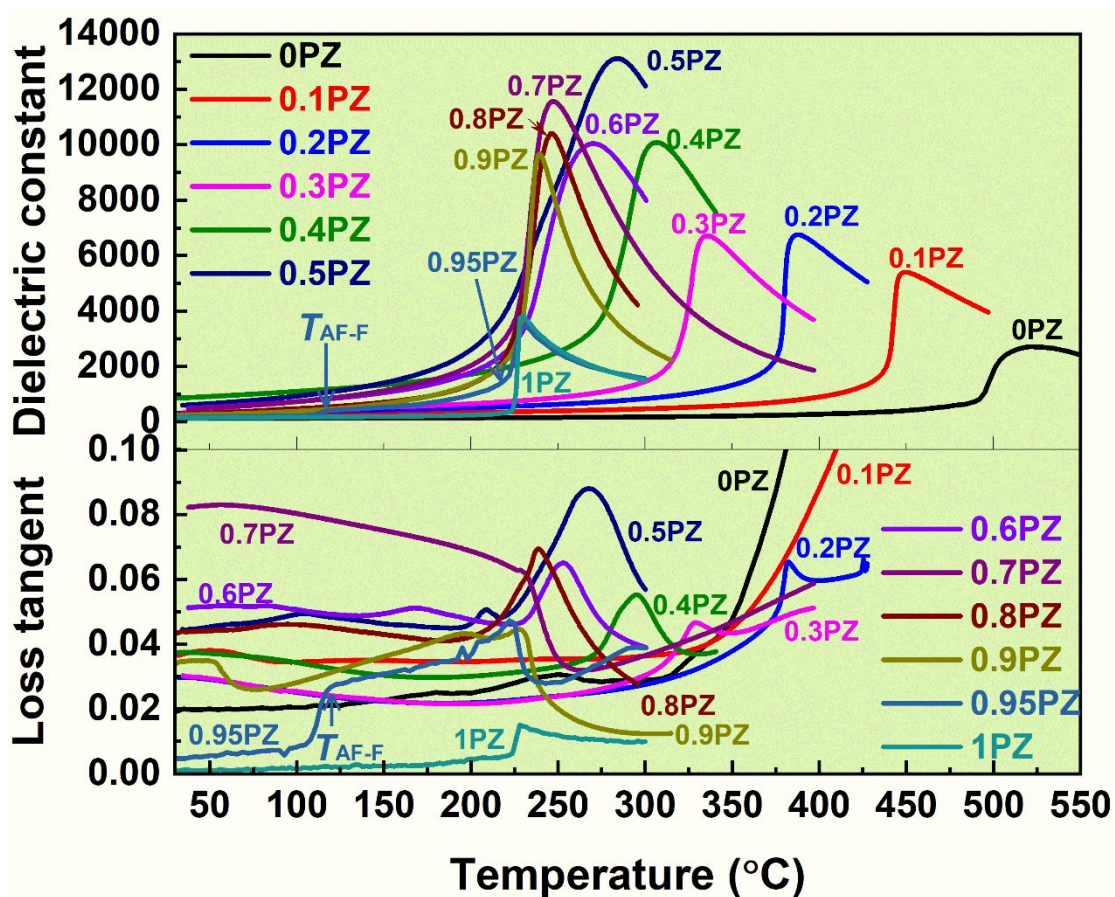


Figure 5. Temperature dependences of the dielectric constant and loss tangent of the  $(1-x)\text{BZNPT}-x\text{PZ}$  ceramics measured at 100 kHz. The phase transition temperatures (Curie temperature  $T_C$  and antiferroelectric to ferroelectric phase transition temperature  $T_{AF-F}$ ) were determined from the temperatures where the dielectric anomaly happens.

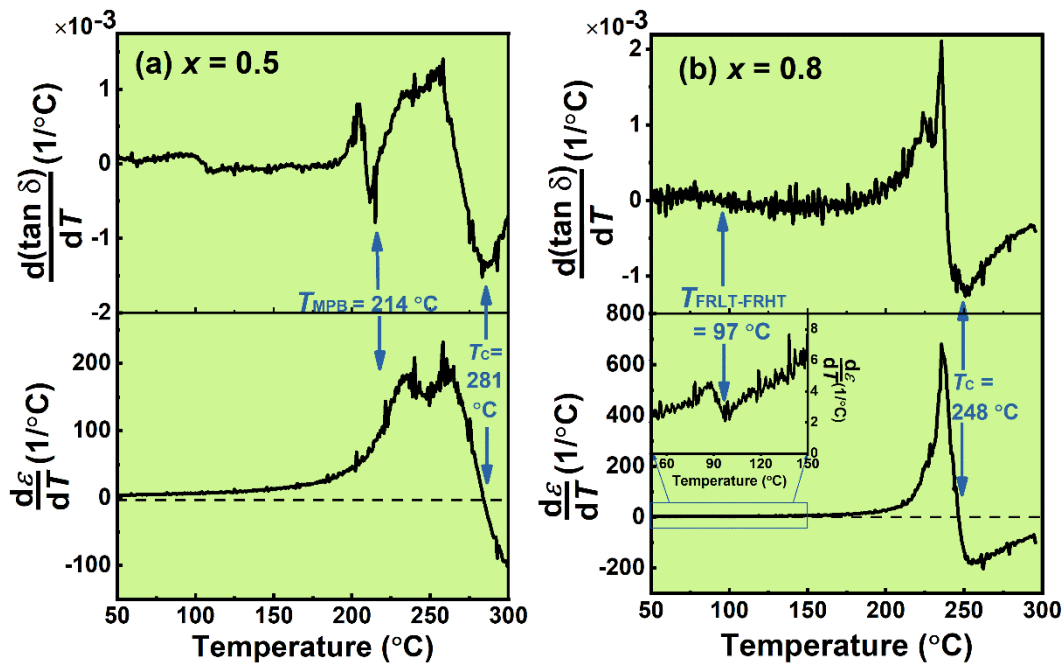


Figure 6. The first-order derivatives of the dielectric constant ( $\varepsilon$ ) and loss tangent ( $\tan\delta$ ) as a function of temperature for (a)  $x = 0.5$  with MPB structure and (b)  $x = 0.8$  with rhombohedral structure at room temperature. The temperature at which  $\frac{d\varepsilon}{dT} = 0$  is identified as  $T_C$  and the local minimum of  $\frac{d}{dT}(\tan\delta)$  and  $\frac{d\varepsilon}{dT}$  is defined as the phase transition temperature at the MPB  $T_{MPB}$  for the MPB composition, and low temperature to high temperature phase transition temperature in the rhombohedral crystal  $T_{FRLT-FRHT}$  for the rhombohedral composition, respectively. More detailed explanations can be found in Ref. 28.

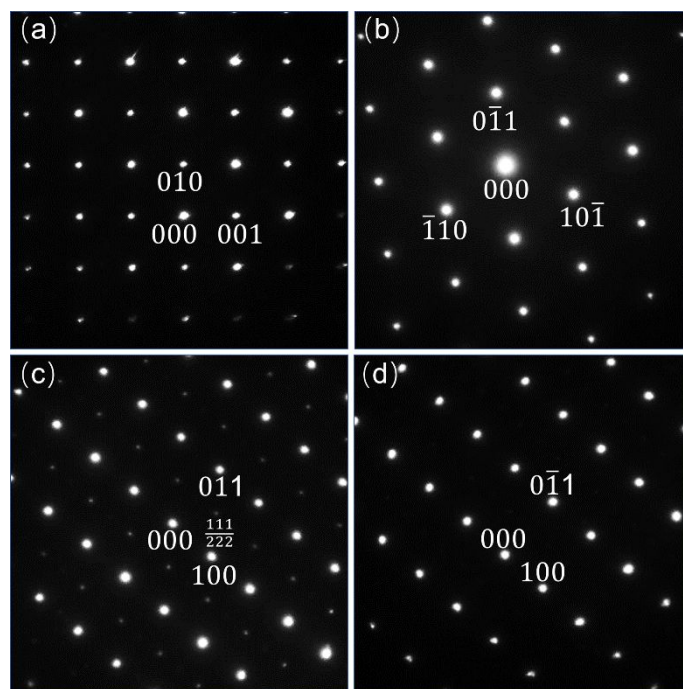


Figure 7. (a)  $[100]_c$ , (b)  $[111]_c$ , (c)  $[0\bar{1}1]_c$  and (d)  $[011]_c$  zone axis electron diffraction pattern obtained from of a sample of 0.3BZNPT-0.7PZ at room temperature.

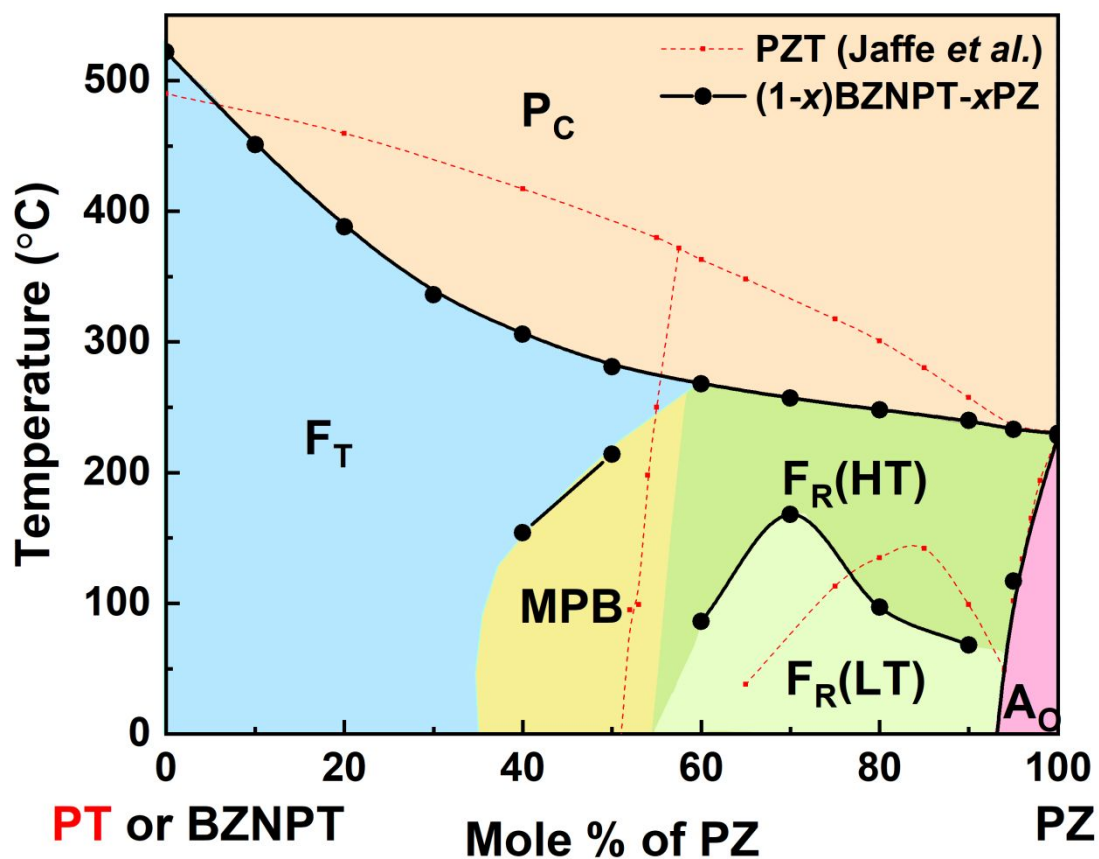


Figure 8. Phase diagram of the  $(1-x)\text{BZNPT}-x\text{PZ}$  pseudo-binary system established from the crystal structural analysis and the dielectric spectrum analysis. For comparison, the data of PZT system obtained by Jaffe *et al.*<sup>11</sup> were also given. The marked phase regions are cubic paraelectric phase  $P_C$ , orthorhombic antiferroelectric phase  $A_O$ , tetragonal ferroelectric phases  $F_T$ , low temperature rhombohedral phase  $F_R(\text{LT})$ , high temperature rhombohedral phase  $F_R(\text{HT})$ , and the morphotropic phase boundary MPB using the notation from Jaffe *et al.*'s work.

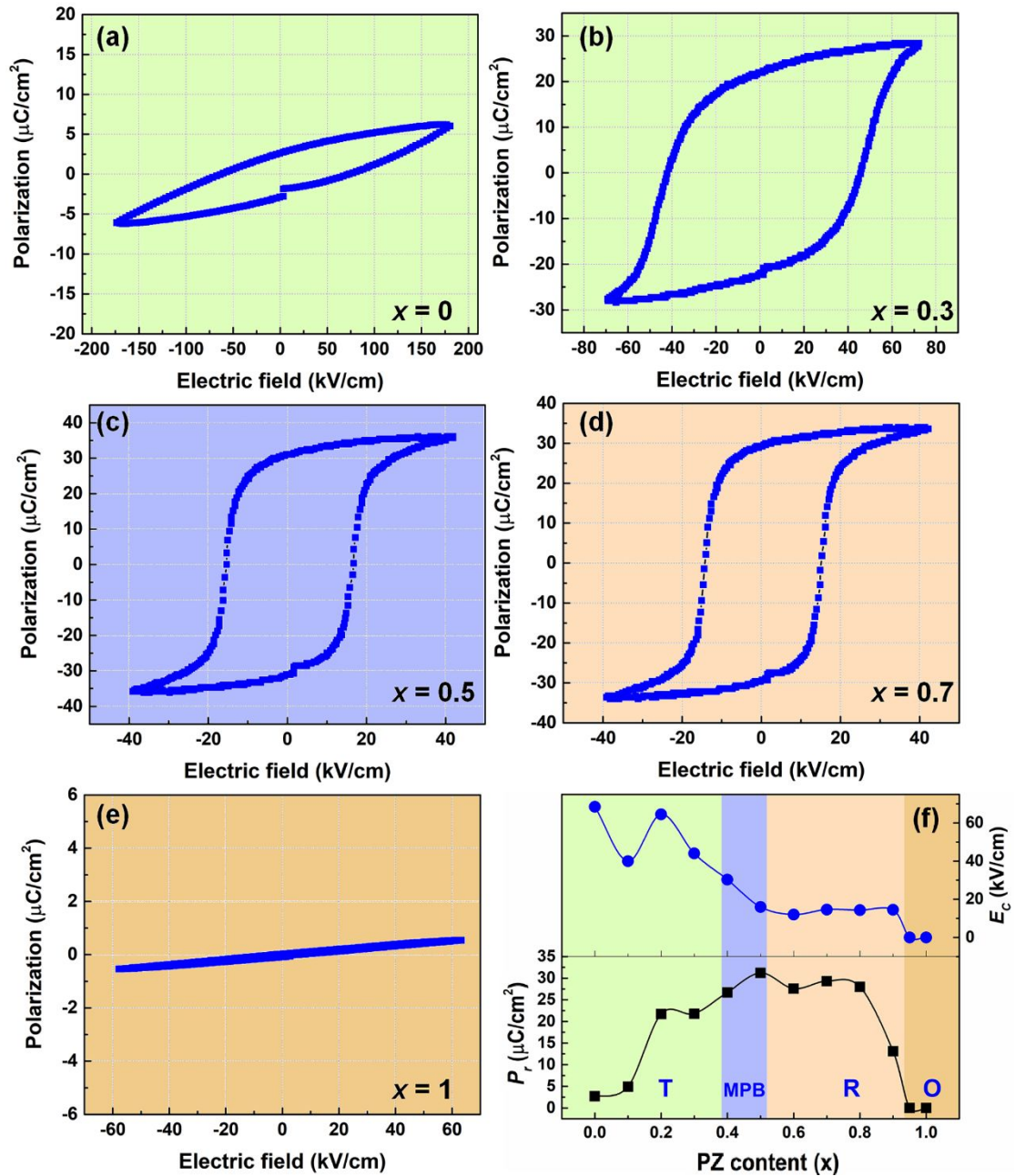


Figure 9. Ferroelectric properties of the  $(1-x)\text{BZNPT}-x\text{PZ}$  ceramics measured at room temperature at 10 Hz: (a)-(e) Polarization versus electric field  $P(E)$  loops at the compositions of  $x = 0$ ,  $x = 0.3$ ,  $x = 0.5$ ,  $x = 0.7$  and  $x = 1$ , respectively. (f) Variations of the remnant polarization ( $P_r$ ), and coercive field ( $E_c$ ) of the  $(1-x)\text{BZNPT}-x\text{PZ}$  ceramics as a function of PZ content.

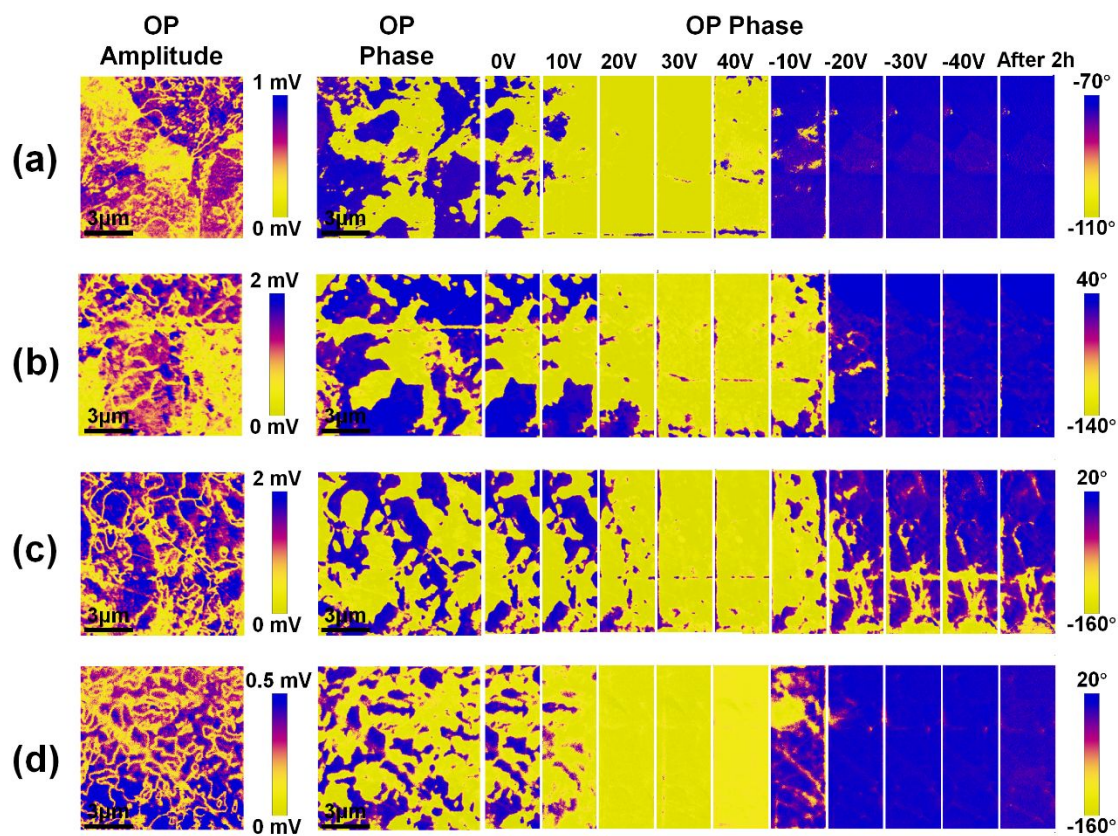


Figure 10. Polar domain structure and its evolution under electric field determined by piezoresponse force microscopy for the (a)  $x = 0.3$ , (b)  $x = 0.4$ , (c)  $x = 0.5$  and (d)  $x = 0.6$  ceramics of the  $(1-x)\text{BZNPT}-x\text{PZ}$  solid solutions.

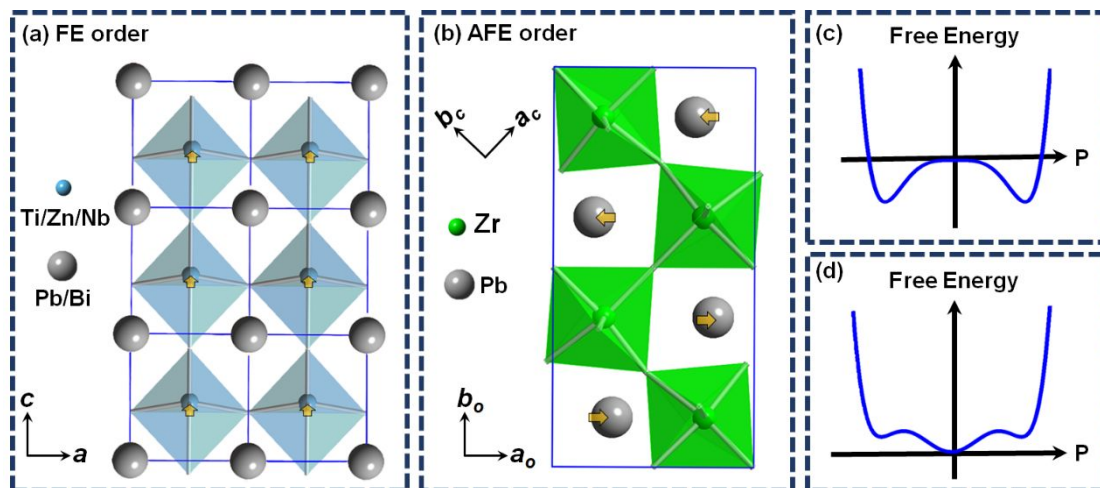


Figure 11. Ferroelectric and antiferroelectric ordering in  $ABO_3$  perovskites: (a) the structure of tetragonal  $0.2\text{Bi}(\text{Zn}_{2/3}\text{Nb}_{1/3})\text{O}_3-0.8\text{PbTiO}_3$  with B-site cations off-center displacement along  $c$ -axis, (b) the structure of orthorhombic  $\text{PbZrO}_3$  with antiparallel displacement of  $\text{Pb}^{2+}$  along the pseudocubic  $[110]_C$  direction, and the schematic Landau potential curves in (c) ferroelectric and (d) antiferroelectric materials.



Novel ferro-/piezoelectric solid solutions between bismuth-based perovskite and antiferroelectric materials are designed. Their crystal structure, phase transition, ferro-/piezoelectric properties and local polar structure are investigated in detail.